Journal of Inorganic and Organometallic Polymers and Materials (2023) 33:120–137
https://doi.org/10.1007/s10904-022-02483-x

Synthesis, Ligating Properties, Thermal Behavior, Computational and Biological Studies of Some Azo-transition Metal Complexes

Mamdouh S. Masoud[1] · Sokaina S. Hemdan[1,2] · Rehab M. I. Elsamra[1]

Received: 20 May 2022 / Accepted: 26 August 2022 / Published online: 16 September 2022

Abstract

Synthesis of new Fe(III), Co(II), Ni(II), and Cu(II) complexes of two azo ligands; 1-(phenyldiazenyl) naphthalene-2-ol (sudan orange R, HL^1), and sodium 2-hydroxy-5-[(*E*)-(4-nitrophenyl) diazenyl]benzoate (alizarin yellow GG, HL^2) have been reported. Stoichiometries of 1:2 and 1:3 (M:L) of the synthesized complexes were approved by total-reflection X-ray fluorescence technique (TXRF) and by elemental analyses. The geometry of complexes (octahedral and square planar) was typified by various spectroscopic, thermal, and magnetic techniques. The ESR spectroscopy showed that Cu(II) complexes are of different isotropic and rhombic symmetries with the existence of Cu–Cu ions interaction. TGA, DTA, and DSC analyses supported the multi-stage thermal decomposition mechanisms, where the thermal breakdown is ended by the formation of metal oxide in most cases. Moreover, chemical reactivity modeling using the density functional theory (DFT) method with the B3LYP/6–31 basis set, showed that metal complexes are more biologically active than their precursor ligands. The calculated lipophilicity character for metal complexes is in the range of 33.8–37.5 eV. Docking results revealed high scoring energy for $[Fe(HL^2)_3].H_2O$ complex and moderate inhibition strength of $[Cu(L^1)_2].H_2O$ complex versus 1bqb, 3t88, and 4esw proteins. Ultimately, the extent of biological effectiveness was endorsed experimentally against four microbial strains. The results are guidelines for toxicological investigations.

✉ Rehab M. I. Elsamra
rehab_elsamra@alexu.edu.eg

[1] Department of Chemistry, Faculty of Science, Alexandria University, Alexandria, Egypt

[2] Department, Factually of Science and Art El Marj, Benghazi University, El Marj, Libya

Graphical Abstract

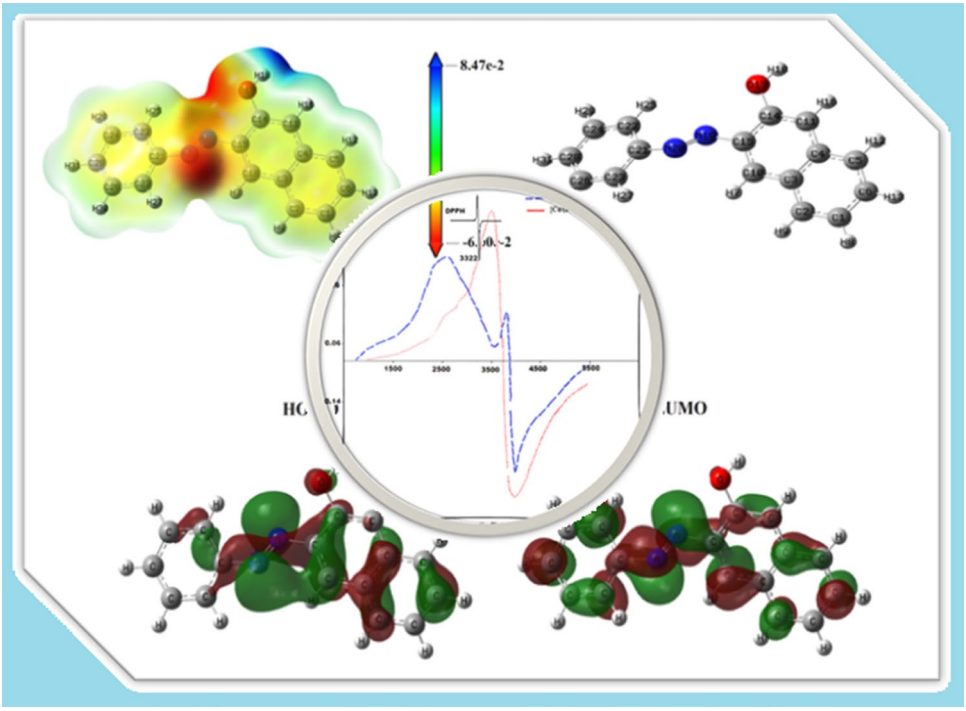

Keywords Azo complexes · Coordination modes · Thermal studies · MOE-docking · Antimicrobial

1 Introduction

Azo ligands are a class of compounds extensively used as indicators in analytical chemistry to show different colors in different media. They have an important role in qualitative and quantitative analyses. Most of these compounds possess an azo group conjugated to one or two arenes. The azo group has great interest for various reasons, such as models of biological systems, antifungals, and analytical reagents [1, 2]. Due to the planarity of the azo bridge versus the nonplanarity of the rest of the system, the azobenzene moiety produces a large π-electron transmission effect and leads to high optical activity. Such activity favors the use of azo-benzene compounds as nonlinear optical (NLO) materials [3, 4]. Besides, the (–N = N–) chromophore together with the conjugated system have induced light sensitivity to these compounds and hence they are incorporated in chemosensors and laser technologies [5]. Azo compounds are also engaged in some therapeutic applications due to their considerable DNA binding affinity [6]. Moreover, the coordination of transition metals with azo-containing ligands produces compounds with significant photocatalytic performances [7]. Azo-containing compounds and their metal complexes are reported to be involved in some biological reactions. For example, alizarine yellow GG contains an azo-linked salicylate moiety which has a structural resemblance to the sulfasalazine drug and can interact with the antiporter protein in the cell membrane [8]. Also, sudan orange ligand is a lipophilic compound that has the capability of interacting with serum albumin which induces conformational changes in the structure of albumin [9]. This article is part of continuing investigations of the structural chemistry of biologically active complexes containing pyrimidine, purine, azo, nitro, nitroso, and azo-nitroso chromophoric groups [10–14]. The major interests of this paper are to study the thermal stability and antimicrobial effects of newly synthesized transition metal-azo complexes derived from sudan orange R (HL^1) and alizarin yellow GG (HL^2). The geometry and binding modes were determined by elemental and spectroscopic techniques. The thermal stability was evaluated by studying the decomposition behavior at different temperatures up to 600 ºC. Recently, the *in-silico* study has become an efficient and essential step to prognose the extent of reactivity of designed chemical structures in many research works [15, 16]. As such, molecular docking was implemented against protein receptors to predict the biological feature of the synthesized compounds. Finally, based on the theoretical calculations, complexes were assessed by in vitro study for their antipathogenic

potency against one Gram-positive (*S. Aureus*), one Gram-negative (*E. Coli*), and two fungi (*C. Albicans* and *A. Flavus*) to endorse their biological strength.

2 Experimental

2.1 Materials and Instruments

All starting materials in this work were purchased from Fluka, Sigma, and BDH companies. Transition metal salts and ligands are of high purity; $CoCl_2.6H_2O$ (98%), $NiCl_2.6H_2O$ (99.9%), $CuCl_2.2H_2O$ (99.9%), and $FeCl_3.6H_2O$ (97%), sudan orange I (≥ 95%), and alizarin yellow GG (≥ 90%). The IR of the ligands and their metal complexes were measured by the KBr disc method using Perkin-Eimer (FT-IR system spectrum BX) in the range from 4400–350 cm^{-1}. The electronic spectral data of the solid complexes in DMF were measured using Double beam UV–Vis. spectrophotometer (Jasco-V.530) in the wavelength range of 200–600 nm. X-band electron spin resonance spectra, ESR, were recorded with JES-FE2XG-ESR Spectrometer (JEOL). The *g*-values were determined by comparison with DPPH (Diphenyl-picryl-hydrazide) signal ($g = 2.0037$). Molar magnetic susceptibility, μ_{eff}, was determined at room temperature (298 K) using Faraday's method [17]. The mass spectra of some selected complexes were measured using mass spectrometer (Thermos scientific GCMS, Shimadzu QP2010 Plus) with an Electron Impact Ionization mode (EI) of 70 eV. Thermogravimetric analysis (TGA), differential thermal analysis (DTA), and differential scanning calorimetry (DSC) were performed using a TG-50 ShimaDzu, LINSEIS STA PT 1000 and DSC-60A Shimadzu at a heating rate of 10 °C min^{-1} under nitrogen (20 cm^3 min^{-1}) in a platinum cell under cooling water flow rate of 10 L h^{-1}. Antimicrobial efficiencies of the isolated complexes were tested and measured employing the disc diffusion method, modified Kirby-Bauer, as described previously [11, 18] at the Regional Center for Mycology and Biotechnology, Al-Azhar University. The chemical structures of the investigated azo-ligands are presented in Fig. S1.

2.2 Synthesis of Metal Complexes

All the metal complexes were prepared in a similar manner, where a required mass equivalent to 10 mmol of transition metal chloride salt: $CoCl_2.6H_2O$ (2.37 g), $NiCl_2.6H_2O$ (2.37 g), $CuCl_2.2H_2O$ (1.70 g) and $FeCl_3.6H_2O$ (2.70 g) was dissolved in (20 ml) distilled water. Solution of the ligand in ethanol was added quantitatively to the metal chloride solution to obtain different (M:L) stoichiometries; (1:2) for Co^{2+}, Ni^{2+} and Cu^{2+} while (1:3) for Fe^{3+}. The reaction mixture was refluxed for 2 h, then cooled. The resulting complexes were filtered and dried at ~ 90 °C. The metal contents of the synthesized complexes were analyzed by three different techniques: the total-reflection X-ray fluorescence (TXRF), [19] atomic absorption spectrophotometric technique (AAS) and titrimetrically with standard EDTA solution using the appropriate indicator. The complexes are synthesized according to Schemes (1 and 2).

2.3 Theoretical Approach

Geometry optimization of selected synthesized compounds was achieved using Gaussian 09 software with Gaussian view for visualization and schematic numbering. The preferred conformers with the minimum energy were obtained by DFT with B3LYP/6-31G base-set without constraining the symmetry [20]. The yielded molecular indices gave excellent predictions about the chemical and biological features of the investigated compounds. Moreover, the ligand–protein receptor binding model for complexes was developed by the MOE-2015 software package. Three protein receptors have been chosen from the Protein Data Bank; 1bqb, 3t88, and 4esw which are corresponding to the three-dimensional crystal structures of *S. Aureus*, *E. Coli*, and *C. Albicans* proteins, respectively [21–23]. Protein repair steps were staged before docking including the elimination of solvent molecules, the addition of hydrogens, chain fixation and selection of active sites of the protein backbone. Also, the tested compounds were oriented for docking by energy minimization, potential energy adaption, atomic charge and binding energy calculations using Merck Molecular Force Field, MMFF94x. This field has been approved to be satisfactory in dealing with a broad range of diverse structural arrangements to evaluate the stability of H-bonds and van der Waals adducts [24] Among thirty ligand-receptor poses, five conformers were selected which represent the best-implanted ligand molecule inside the protein active pocket with bond lengths less than 3.5 Å and of highest scoring energy.

3 Results and Discussion

Seven complexes derived from HL^1 and HL^2 azo-ligands are synthesized. The complexes are characterized by spectroscopic (IR, UV–Vis, ESR), thermal (TGA, DTA, DSC) and magnetic susceptibility measurements. Also, Molecular geometry and electronic parameters are determined by the DFT method of calculation.

3.1 Characterization of the Complexes

3.1.1 FT-IR Study

The FT-IR spectra of the investigated azo-ligands and their complexes were studied to characterize the mode of bonding

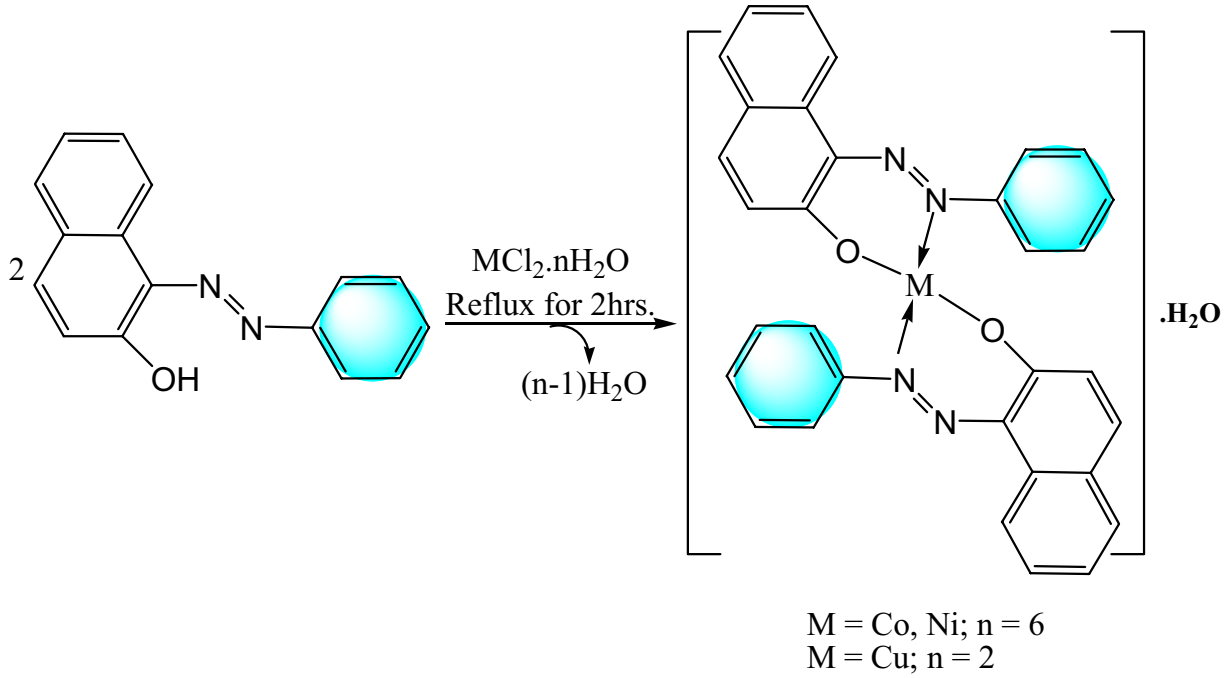

Scheme 1 Synthesis of metal complexes derived from HL^1

between the metal ion and the ligand (Table S1 and Figs. 1, S2). The IR spectrum of the HL^1 free ligand exhibited bands at 3462, 1622, 1499, 1449, 1321 and 1208 cm^{-1}, which are assigned to ν_{OH}, $\nu_{C=C}$, ν_{C-C}, $\nu_{N=N}$, ν_{C-N}, and ν_{C-O} vibrational modes, respectively [25]. The characteristic infrared spectral band of HL^1 complexes (Fig. S2) showed a remarkable change in the intensity and slight shift in the position of $\nu_{N=N}$ bands upon complexation. Besides, the disappearance of the ν_{OH} bands in the IR spectrum of the complexes (Fig. S2) suggests the deprotonation of the phenolic OH group. Noteworthy, the broadband that appeared in the region > 3300 cm^{-1} in the IR spectrum of the HL^1 complexes could be attributed to the water of crystallization which is approved later by thermal analysis. Accordingly, HL^1 behaves as a bidentate ligand, coordinating via the oxygen atom of the OH group in the naphthalene moiety after a loss of proton and the lone pair of electrons on the nitrogen of the azo group forming a stable six-membered ring. This mode of coordination is supported by the disappearance or lowering in the intensity of the bands due to bonded OH group [26] and the stretching frequency of the azo-group with the simultaneous appearance of new bands in the frequency ranges 608–557 cm^{-1} and 497–371 cm^{-1} of ν_{M-O} and ν_{M-N}, respectively [27].

Likewise, the characteristic ν_{OH} band at 3468 cm^{-1} for the free ligand HL^2 was slightly shifted in all complexes (Table S1 and Fig. 1) indicating the involvement of the OH group in the complex formation without deprotonation. The ν_{C-O} band at 1390 cm^{-1} in the free ligand exhibited a considerable change in the position and intensity upon complexation indicating the contribution of the carboxylic oxygen in the complex formation [28]. Additionally, the bands due to the scissoring and wagging of the carboxylate group in the range 900–600 cm^{-1} displayed noticeable changes in their intensities [29]. The band at 1495 cm^{-1} of the free ligand spectrum is due to the stretching vibration of the azo group, $\nu_{N=N}$, in an azobenzene-like structure in a trans configuration [30]. The $\nu_{N=N}$ band is nearly unaffected through complexation which rules out the participation of the azo group in the chelation. The asymmetric and symmetric stretching vibrations of the carboxylate group at 1540 and 1410 cm^{-1}, respectively [31], appeared clearly in all HL^2-complexes, implying the involvement of this group in the chelation moiety. Hence, all HL^2-complexes are neutral, where the charge on the central metal ion is balanced by binding to the COO^- groups of the coordinated ligands (Fig. 1).

3.1.2 UV–Vis, NMR, MS, and Magnetic Susceptibility Studies

The UV–Vis. spectrum of the HL^1-metal complexes showed three electronic absorption bands at 268, 308–320, 370–478 nm in DMF (Table 1 & Figs. S3–S6). The band at 268 nm is attributed to $\pi \rightarrow \pi^*$ resulted from the interaction of π-electrons in the conjugated system. Also, the bands in the range 308–320 nm are assigned to $n \rightarrow \pi^*$ developed from the non-bonding electrons on the azo group. However, the intense broad bands in the range 370–478 nm are due to the

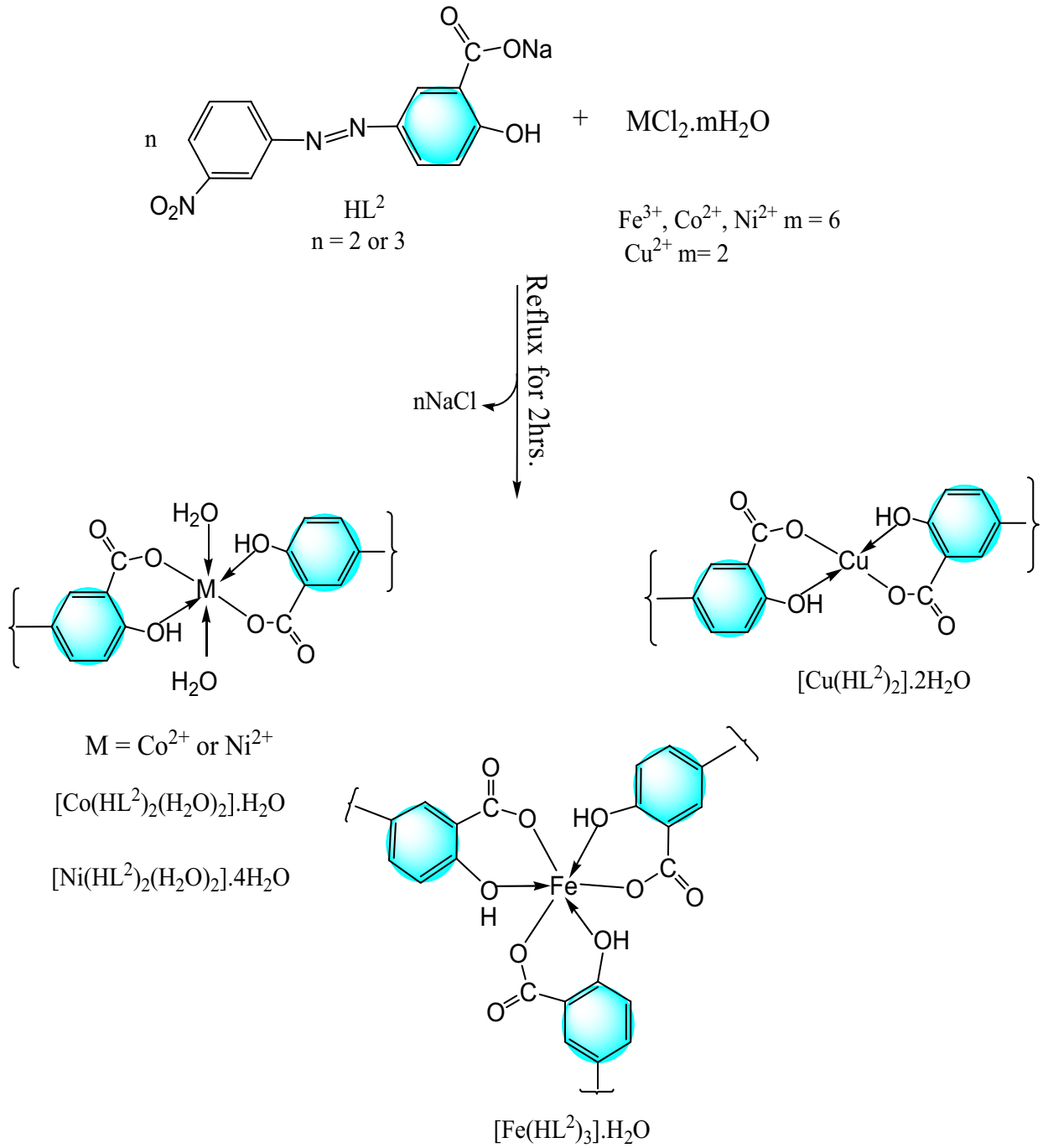

Scheme 2 Synthesis of metal complexes derived from HL^2

charge transfer (CT). The room temperature value of μ_{eff} of $[Ni(L^1)_2].H_2O$ is zero. This diamagnetic behavior indicates the square planar environment around Ni(II) ion of low-spin type. Moreover, the electronic spectral band at 478 nm of the Cu-HL^1 complex, $[Cu(L^1)_2].H_2O$, could be assigned to $^2B_{1g} \rightarrow {}^2B_{2g}$ electronic transition which is concealed by the broad CT transition. Besides, the μ_{eff} values of 1.85 B.M for $[Cu(L^1)_2].H_2O$ and 2.65 B.M. for $[Co(L^1)_2].H_2O$ typified the existence of square planar geometry (Scheme 1) [32, 33]. Furthermore, the electronic absorption spectra of HL^2 complexes in DMF, $[Fe(HL^2)_3].H_2O$, $[Co(HL^2)_2(H_2O)_2].H_2O$, $[Ni(HL^2)_2(H_2O)_2]0.4H_2O$ and $[Cu(HL^2)_2]0.2H_2O$, exhibited different bands, (Table 1). Similarly, the bands at 268 -270 nm for these complexes are assigned to $\pi \rightarrow \pi^*$ transition whereas the bands at higher wavelength, 392–396 nm, are attributed to CT from ligand to metal. The broadness

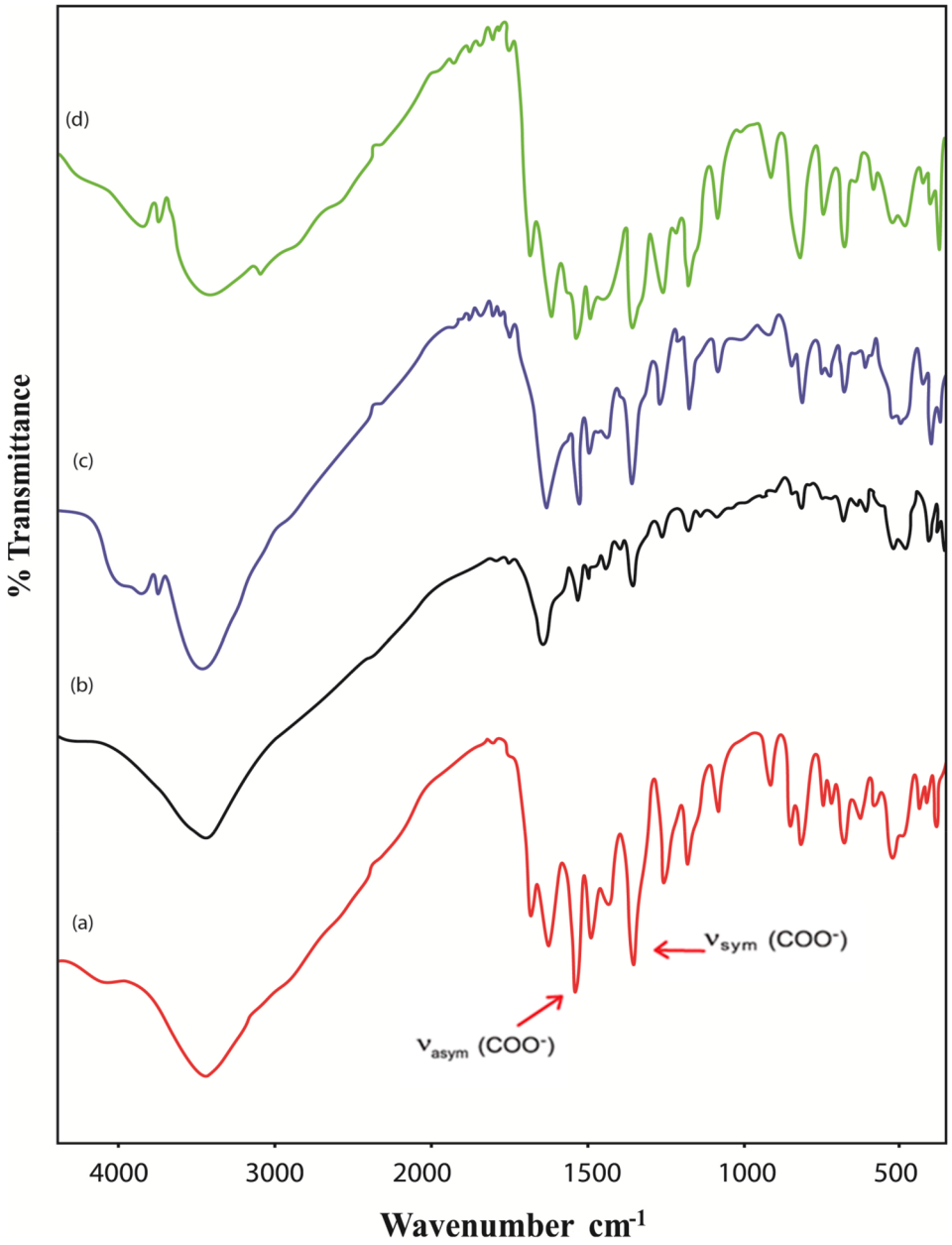

Fig. 1 Infrared spectra of HL^2 metal complexes, **a** $[Fe(HL^2)_3].H_2O$ **b** $[Co(HL^2)_2(H_2O)_2].H_2O$ **c** $[Ni(HL^2)_2(H_2O)_2].4H_2O$ **d** $[Cu(HL^2)_2].2H_2O$

of the CT band obscured the possible d-d transitions of the complexes as $^3A_{2g} \rightarrow {}^3T_{1g}$ (P) in the case of Ni (II) in an octahedral field that lies within the same spectral region. The room temperature μ_{eff} (Table 1) characterizes the octahedral geometry for all HL^2 complexes except $[Cu(HL^2)_2]0.2H_2O$ complex which has $\mu_{eff} = 1.77$ B.M. of square-planar D_2h symmetry [32]. Based on the FT-IR, electronic spectra, and magnetic susceptibility, HL^2 is verified to have a bidentate nature which binds to the metal ion through two oxygen atoms of OH and the COO^- groups. The proposed structures of the isolated complexes from the reaction of sodium salt of alizarin yellow GG with metal chloride are given in Scheme 2. Moreover, ^1H NMR of the free HL^1 ligand ($C_{16}H_{12}N_2O$) showed different types of protons, Fig. 2, where the phenolic OH appeared at the most downfield part of the spectrum at $\delta = 8.49$ ppm. Besides, the aromatic hydrogens appeared in the range (6.87–7.92 ppm). Interestingly, the phenolic OH disappears in the spectrum of the diamagnetic $[Ni(L^1)_2].H_2O$ complex, indicating the deprotonation before complex formation, Fig. S7. The ^1H NMR peak integrations are equivalent to 12 protons. Additionally, ^{13}C NMR of the HL^1 ligand showed 14 peaks corresponding to 16 carbon atoms where two of these peaks represent identical carbon environments, Fig. 3.

The mass spectral data of the synthesized complexes are collected in Figs. 4 and S8–S13. The molecular ion peaks

Table 1 Elemental analysis data, metal content, magnetic moment, (λ_{max}, nm) values and the proposed geometries of the synthesized metal azo-ligand complexes

Complex*	FormulaMwt	% Calculated / (Found)				μ_{eff}B.M	λ_{max}	Geometry
		M	C	H	N			
$[Co(L^1)_2].H_2O$	$C_{32}H_{24}N_4O_3Co$ 571.49	10.31 (10.12)	67.25 (67.49)	4.23 (4.48)	9.80 (9.67)	2.65	268, 320, 370	Square planar
$[Ni(L^1)_2].H_2O$	$C_{32}H_{24}N_4O_3Ni$ 571.25	10.27 (10.52)	67.28 (67.43)	4.23 (4.42)	9.81 (9.85)	dia	268, 312, 478	Square planar
$[Cu(L^1)_2].H_2O$	$C_{32}H_{24}N_4O_3Cu$ 576.10	11.03 (11.12)	66.71 (66.43)	4.20 (4.51)	9.73 (9.95)	1.85	268, 308, 478	Square planar
$[Fe(HL^2)_3].H_2O$	$C_{39}H_{26}N_9O_{16}Fe$ 932.52	5.99 (5.69)	50.23 (50.06)	2.81 (2.64)	13.52 (13.67)	5.93	230, 268, 396	Octahedral
$[Co(HL^2)_2(H_2O)_2].H_2O$	$C_{26}H_{22}N_6O_{13}Co$ 685.42	8.60 (8.87)	45.56 (45.80)	3.24 (3.53)	12.26 (11.97)	4.85	268, 392	Octahedral
$[Ni(HL^2)_2(H_2O)_2].4H_2O$	$C_{26}H_{28}N_6O_{16}Ni$ 739.22	7.94 (8.05)	42.24 (42.11)	3.82 (3.66)	11.37 (11.12)	2.97	268, 392	Octahedral
$[Cu(HL^2)_2].2H_2O$	$C_{26}H_{20}N_6O_{12}Cu$ 672.02	9.46 (9.70)	46.47 (46.22)	3.00 (3.27)	12.51 (12.37)	1.77	270, 392	Square planar

* All complexes are of melting points > 300 ºC

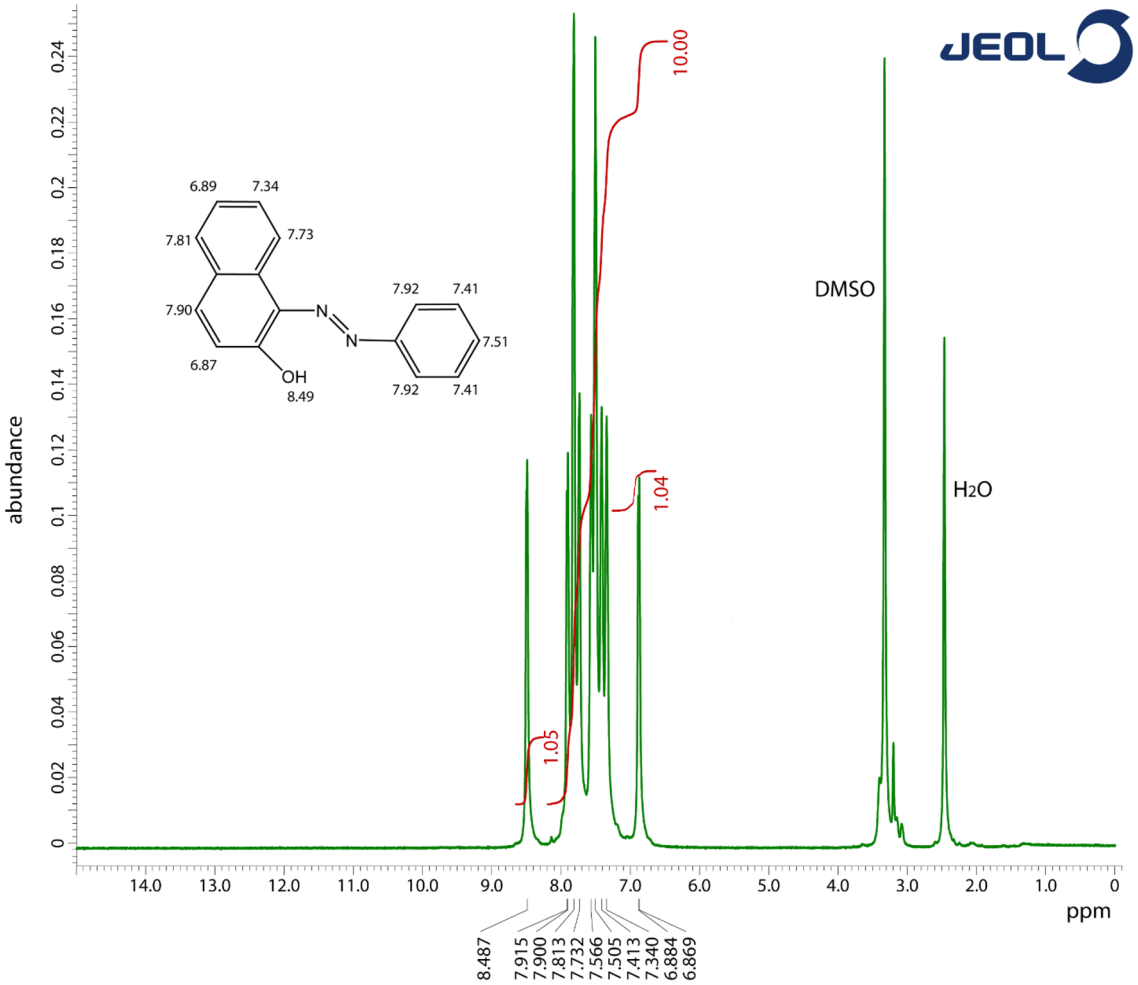

Fig. 2 ^{1}H NMR of the free ligand HL^1 in DMSO

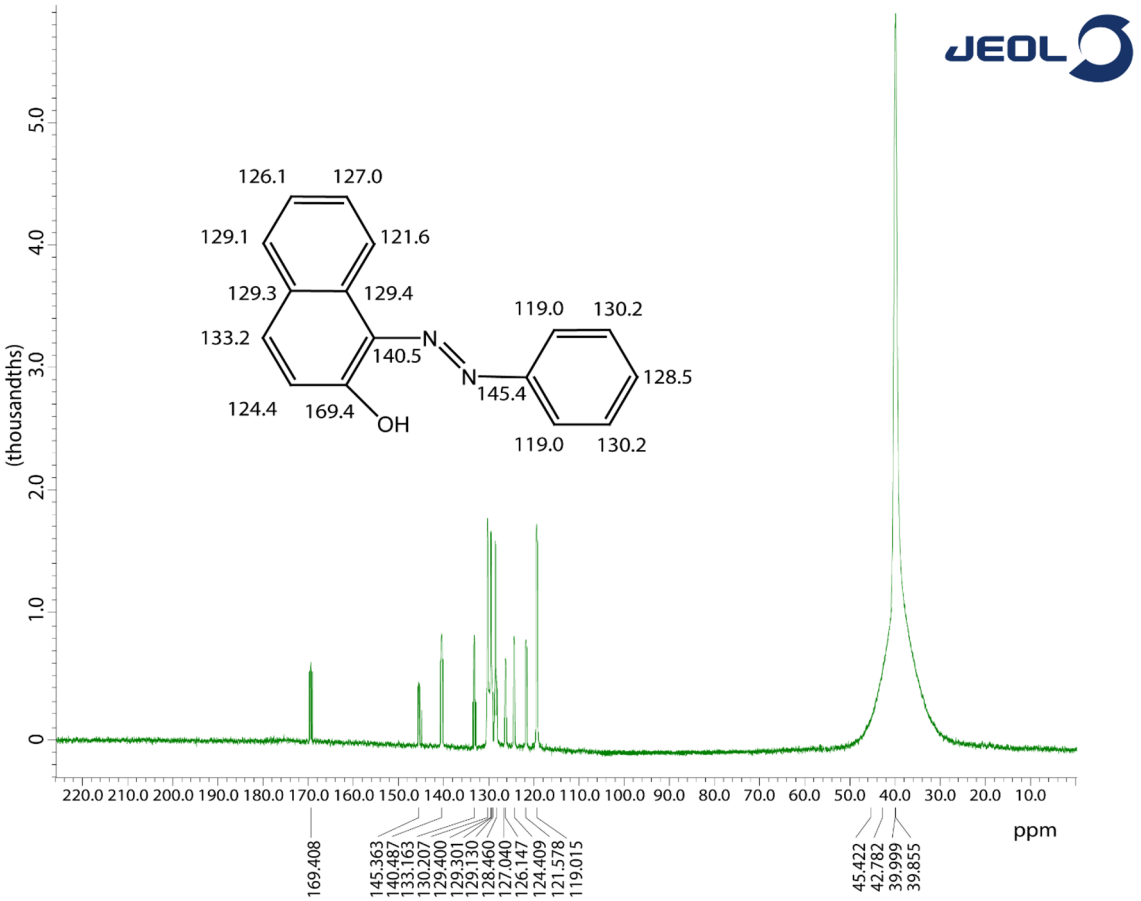

Fig. 3 ^{13}C NMR of the free ligand HL^1 in DMSO

($M^{+\bullet}$) of the synthesized complexes are consistent with their proposed formula. For example, the mass spectrum of $[Cu(L^1)_2].H_2O$ displayed a molecular ion peak at *m/z* 576.14. The spectrum displayed other peaks at *m/z* 558.54, 170.29, 154.95, and 77.67 corresponding to the cationic fragments $[Cu(L^1)_2]^+$, $C_{10}H_6N_2O_2^+$, $C_{10}H_6N_2^+$, and $C_6H_5^+$ respectively. Also, the molecular ion peak of $[Cu(HL^2)_2]0.2H_2O$ complex at *m/z* 672.05 supports its proposed structure. Moreover, the base peaks of $[Cu(L^1)_2].H_2O$ and $[Cu(HL^2)_2]0.2H_2O$ complexes with 100% abundance at *m/z* 126.92 and 286.68 could be assigned to the formula weight of naphthalene and HL^2 cations, respectively, (Figs. 4 and S8). Noteworthy, the mass spectra of other complexes are in excellent agreement with their elemental analyses.

3.1.3 ESR of Copper (II) Complexes

The room temperature X-band powdered electronic spin resonance of the square planar $[Cu(L^1)_2].H_2O$ derived from HL^1 (Fig. 5) showed an anisotropic spectrum of rhombic type [34]. The *g*-values are $g_1 = 2.639$, $g_2 = 1.788$ and $g_3 = 1.741$. The $< g >$ value is equal to 2.056. Here, the deviation of the $< g >$ value from the free electron 2.0032 could be due to the misalignment of the local copper (II) environment and the probability of Cu-Cu ion exchange [32]. The *R*-parameter which is calculated by the relation $R = (g_2 - g_1)/(g_3 - g_2)$ equals to 18.11 ($R > 1$) implying that the ground state is d_z^2 [32]. However, the ESR spectra of the square planar $[Cu(HL^2)_2]\ 0.2H_2O$ complex derived from HL^2 is of isotropic spectral pattern of dynamic or pseudo rotational type of Jahn–Teller distortion (Fig. 5) at $g_{iso} = 1.85$ with $A = 333.33 \times 10^{-4}$ cm^{-1}. Isotropic spectrum is common for complexes containing misaligned "tetragonal" axes of magnetically dilute interaction [34]. The observed broadening of the resonance line suggests a heightened magnetic dipole interaction between the paramagnetic centers due to the polymeric nature of this complex [35].

3.1.4 Thermal Analysis (TGA, DTA, and DSC)

The TGA curves for the investigated azo-ligands and their complexes are collected in Figs. 6 & S14. The thermal decomposition pattern and assignment of the removed species are presented in Tables 2 & S2. A slight difference was

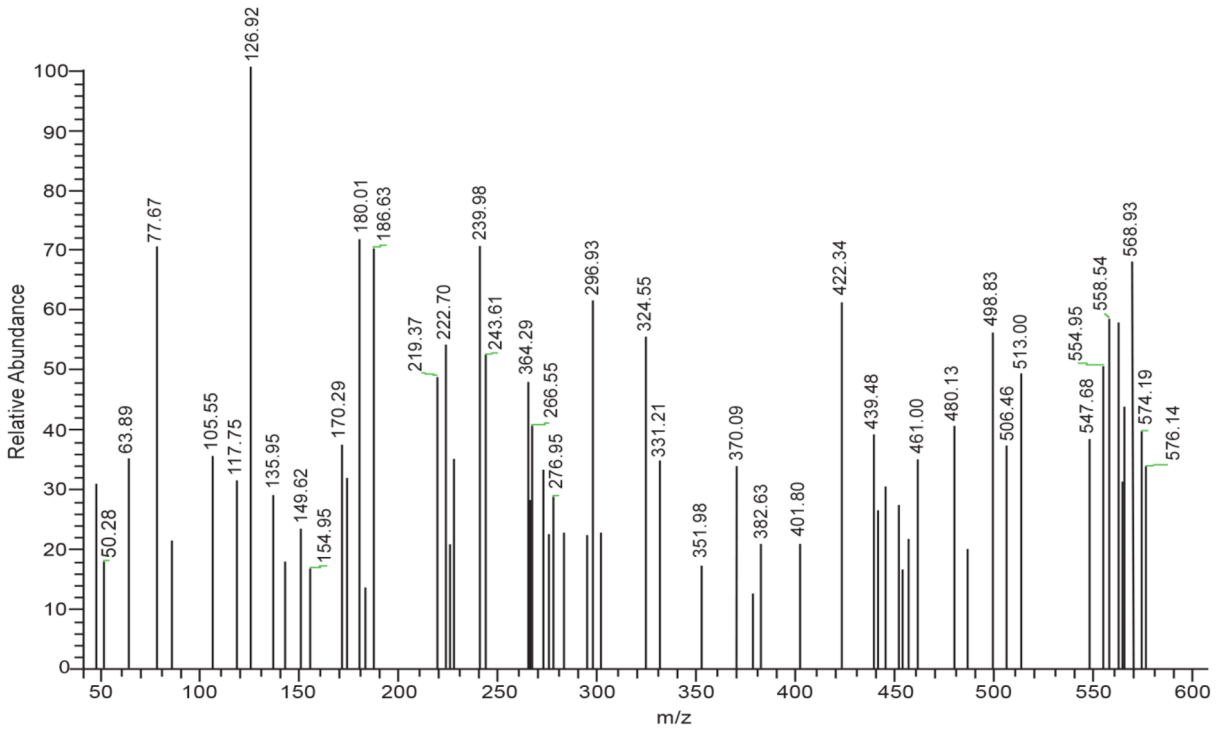

Fig. 4 Mass spectrum of $[Cu(L^1)_2].H_2O$ complex

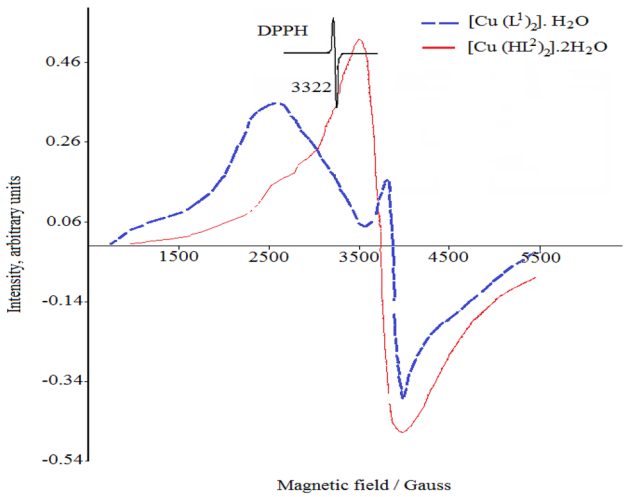

Fig. 5 X-band ESR spectra of Cu(II) complexes

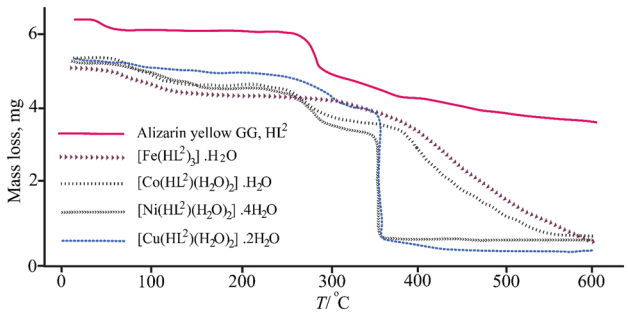

Fig. 6 TGA curves of HL^2 and its metal complexes

discerned between the found and calculated mass percentage which points to the overlapping between some of the successive steps. This overlapping is further supported by the observed DTA peak temperature value, T_m, corresponding to each TGA step temperature range, (Tables 2 & S2). The TGA thermogram of HL^1 complexes, $[Co(L^1)_2].H_2O$, $[Ni(L^1)_2].H_2O$, and $[Cu(L^1)_2].H_2O$ specifies their thermal stability up to ~ 200 °C. The removal of water of crystallization from the complexes starts at low temperatures but extended to ~ 189 °C (Fig. S14). This may be attributed to a strong attachment of the outer sphere H_2O to the coordination sphere through hydrogen bonds which delays its removal during the thermal decomposition [36].

Generally, the thermal decomposition routes of the complexes proceed in three main stages where the bond between the central metal ion and the ligands starts to dissociate after losing small molecules such as H_2O, NO_2, and CO_2 (Tables 2 & S2). The thermal decomposition of the larger fragment of the ligand is noticed in the second stage which takes place in two steps as in $[Fe(HL^2)_3].H_2O$ or three successive steps as in $[Ni(L^1)_2].H_2O$ case, Fig. S14. The final stage is assigned to the liberation of the rest of the ligands

Table 2 DTA and TGA analyses of HL^2-metal complexes

Compounds	Type	T_m(°C)	Temp. (°C) TGA	Wt. loss%		Removed species
				Found	Calc	
$[Fe(HL^2)_3].H_2O$	Exo	99.7	47.4–155.2	12.11	11.80	H_2O, $2NO_2$
			204.7–232.8	5.10	4.93	NO_2
	Exo	318.5	280.2–599.6	70.12	70.84	$C_{38}H_{24}N_6O_6$
			Residue	12.67	12.42	$FeCO_3$
$[Co(HL^2)_2(H_2O)_2].H_2O$	Endo	small	63.6–158.7	7.51	7.89	$3H_2O$
	Endo	broad	239.5–327.0	20.57	19.84	$2NO_2$, CO_2
	Exo	379.6	353.3–548.4	61.19	61.34	$C_{25}H_{16}N_4O_3$
			Residue	10.73	10.93	CoO
$[Ni(HL^2)_2(H_2O)_2].4H_2O$	Exo	88.7	34.8–161.0	11.86	12.19	$5H_2O$
	Exo	broad	229.4–325.0	21.07	20.84	H_2O, $2NO_2$, CO_2
	Exo	355.7	325.0–430.3	56.99	56.87	$C_{25}H_{16}N_4O_3$
			Residue	10.08	10.10	NiO
$[Cu(HL^2)_2].2H_2O$	Exo	106.2	40.3–131.4	5.42	5.36	$2H_2O$
			220.4–333.5	20.17	20.24	$2NO_2$, CO_2
	Exo	365.5	333.5–439.5	62.31	62.56	$C_{25}H_{16}N_4O_3$
			Residue	12.10	11.84	CuO

as free radical species ended with metal oxide residue in most cases. Moreover, the formation of metal carbonate as a residue in the thermal decomposition of $[Fe(HL^2)_3].H_2O$ (Fig. 6 and Table 2) supports the bonding of the Fe(III) to the carboxylate group as indicated in the spectral data and similarly reported complexes in literature [37].

The DTA curves for the entitled azo-ligands and some of their complexes are presented in Figs. 7 & S15-S18. The considerably high thermal stability of some complexes was directly inferred from the first decomposition DTA peak maximum (T_m), Table 2, which corresponds to the start of the metal–ligand bond breaking. For example, $[Ni(HL^2)_2(H_2O)_2]0.4H_2O$ complex possesses high thermal stability as the metal–ligand bond starts to break in the range 325.0–430.3 °C with a T_m of 355.7 °C. The DTA Curve for Ni-HL^1 complex, $[Ni(L^1)_2].H_2O$ (Fig. 7) exhibits an exothermic peak at 92.0 ºC corresponding to the dehydration of water molecule from the outer sphere of the complex. Two small exothermic steps are observed in the range 293.6–355.6 ºC assigned to the fragmentation

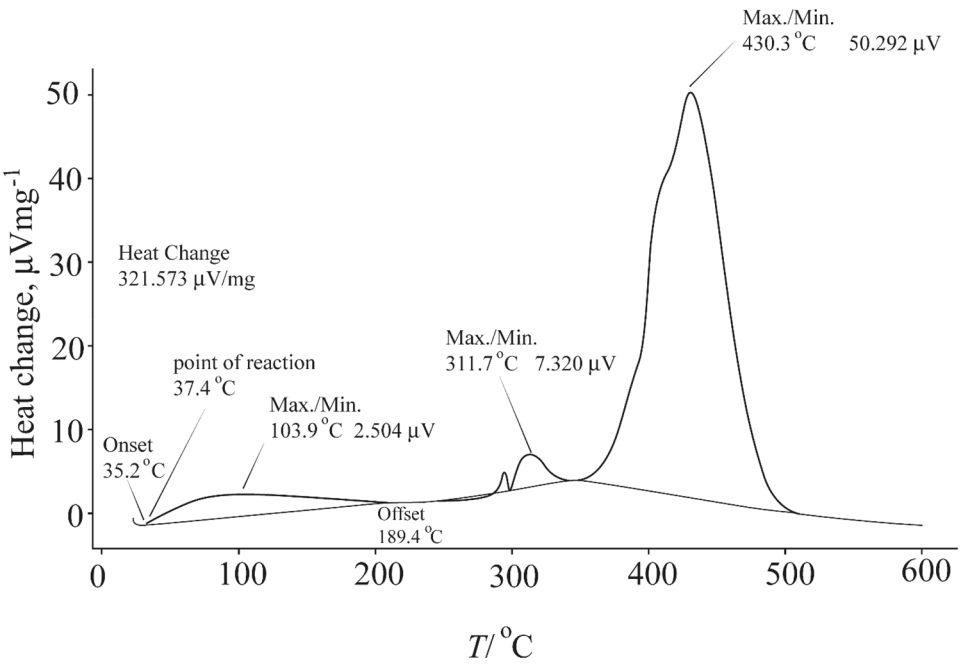

Fig. 7 DTA Curve for $[Ni(L^1)_2].H_2O$ complex

of the phenyl groups. The last stage is accompanied by an exothermic peak at 430.3 ºC due to the liberation of the naphthalene moieties of the ligand which is ended with the formation of NiO as a final product [38]. The exothermic nature of the thermal decomposition steps of $[Ni(L^1)_2].H_2O$ complex is verified by the positive direction of DTA curves (Fig. 7). Also, the DTA curve for Fe-HL^2 complex, $[Fe(HL^2)_3].H_2O$ (Fig. S15) exhibits an exothermic peak at 99.7 ºC corresponding to two TGA steps assigned to dehydration of one water molecule in the atmosphere of the complex, and the loss of 2 NO_2. The last step appeared as an exothermic peak at 318.5 ºC assigning the liberation of the rest of the ligand which ended with the formation of $FeCO_3$.

The DSC measurements for HL^2 and its Ni-complex, $[Ni(HL^2)_2(H_2O)_2]0.4H_2O$, were carried out under a flow of N_2 at a heating rate of 10 °C min^{-1} in the temperature range of 25–200 °C. Apparently, both HL^2 and its Ni-complex exhibited distinct transitions from glassy disordered to the more ordered crystalline solid phase. HL^2 displayed a glass transition temperature, T_g, at 57 °C (Fig. 8). This temperature represents the change in the heat capacity of the disordered solid without exhibiting any phase transition. However, $[Ni(HL^2)_2(H_2O)_2]0.4H_2O$ complex showed a higher glass transition temperature, $T_g = 85$ °C, than the free ligand owing to the decrease in the free space of the complex as a result of coordination to the metal ion [39]. The crystallization temperature, T_c, which is indicative of the transition from disordered to crystalline solid, appeared at 135 and 149 °C for HL^2 and its Ni-complex respectively. The melting process of the investigated compounds was not discerned within the studied temperature range (25–200 °C). The melting temperatures are 274 °C for HL^2 and > 300 °C for the Ni-complex as measured experimentally by Fisher-Johns melting-point apparatus. The elevated melting point values further support the thermal stability of the synthesized complexes up to at least 300 °C (Tables 1 and 2).

3.2 Computational Analysis

Optimization of the geometrical structures of all studied compounds to their minimum energy values was achieved using the density functional theory (DFT) method of calculation with B3LYP/6-31G basis sets. Electrophilic and nucleophilic regions on the ligand's surfaces were evaluated aiming to investigate the optimal binding sites for the interactions with metal ions that were proposed experimentally in this contribution. Also, the stability of the square planar and octahedral geometries of complexes was examined by DFT calculations without enforcing symmetry around the metal centers. The yielded data are displayed in Tables 3, S3-S5, Figs. 9, 10, 11 & S19-S23.

3.2.1 Molecular Geometry and Electronic Parameters

The optimization of geometries of HL^1, HL^2 and their metal complexes by DFT calculation provided different possible conformers with diverse bond angles and bond lengths. The most stable conformers, i.e. the ones with the minimum structural energy, are given in Figs. 9 & S19-S21. The bond lengths of the functional groups of the optimized structure of HL^1 are stated in Table S3 as a representative example. Noticeably, the sites of coordination of HL^1 with the metal ion in $[Cu(L^1)_2].H_2O$ complex (Table S4) exhibited slight elongation in the bond length relative to the free HL^1 (Table S3) as presented in Fig. 9. Besides, Cu(II) in $[Cu(L^1)_2].H_2O$ complex is coordinated to N(20) and N(50) of the azo groups with an average Cu(1)–N bond length of 1.94 Å and O(19) and O(49) with a Cu(1)–O bond length of 1.85 Å. The bond angles in the coordination sphere around Cu(II) are 95.73º and 92.33º for N(20)–Cu(1)–O(49) and N(50)–Cu(1)–O(49) respectively (Table S4). This finding

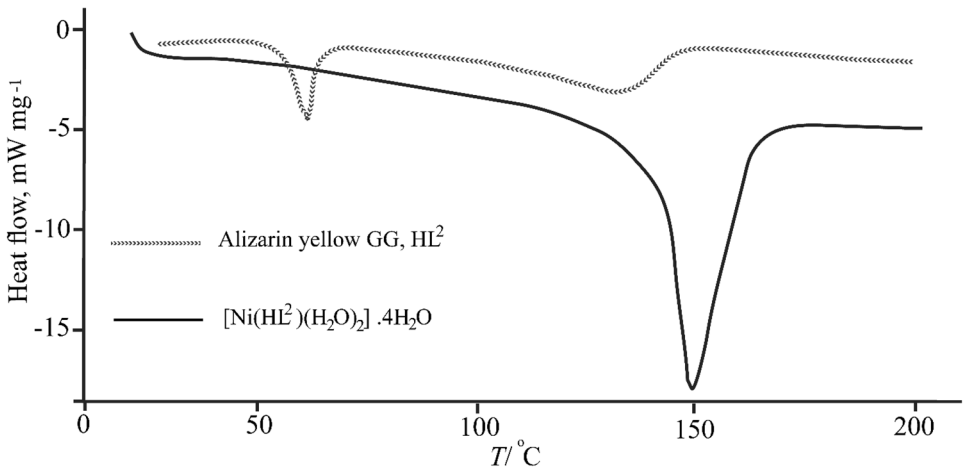

Fig. 8 DSC-Curve for HL^2 and its Ni (II) complex

points to the square planar geometry around Cu(II) center, with a small discrepancy of 2-5º from the ideal square planar angles (90º) probably due to the bulkiness of the ligand structure [40, 41]. Moreover, the molecular properties of the studied compounds such as the energies of the highest occupied (E_{HOMO}) and the lowest unoccupied (E_{LUMO}) molecular orbitals (Figs. 10 and S22) as well as the chemical reactivity parameters; electronegativity (χ), electrochemical potential

Table 3 The calculated molecular parameters of HL^1, HL^2 and the synthesized metal complexes of HL^1

Compound	Total Energy (Hartree)	Dipole moment (Debye)	E_{HOMO} (eV)	E_{LUMO} (eV)	ΔE (eV)	η (eV)	S (eV^{-1})	μ (eV)	χ (eV)	ω (eV)
HL^1	− 801	1.087	− 5.550	− 2.004	3.546	1.773	0.282	− 3.777	3.777	4.023
HL^2	− 1040	14.68	− 2.537	− 0.832	1.705	0.853	0.586	− 1.685	1.685	1.664
$[Cu(L^1)_2].H_2O$	− 3242	0.551	− 8.531	− 6.937	1.594	0.797	0.627	− 7.734	7.734	37.52
$[Co(L^1)_2].H_2O$	− 3105	0.682	− 8.566	− 6.815	1.751	0.876	0.571	− 7.691	7.691	33.76
$[Ni(L^1)_2].H_2O$	− 3111	0.591	− 8.522	− 6.912	1.610	0.805	0.621	− 7.717	7.717	36.99

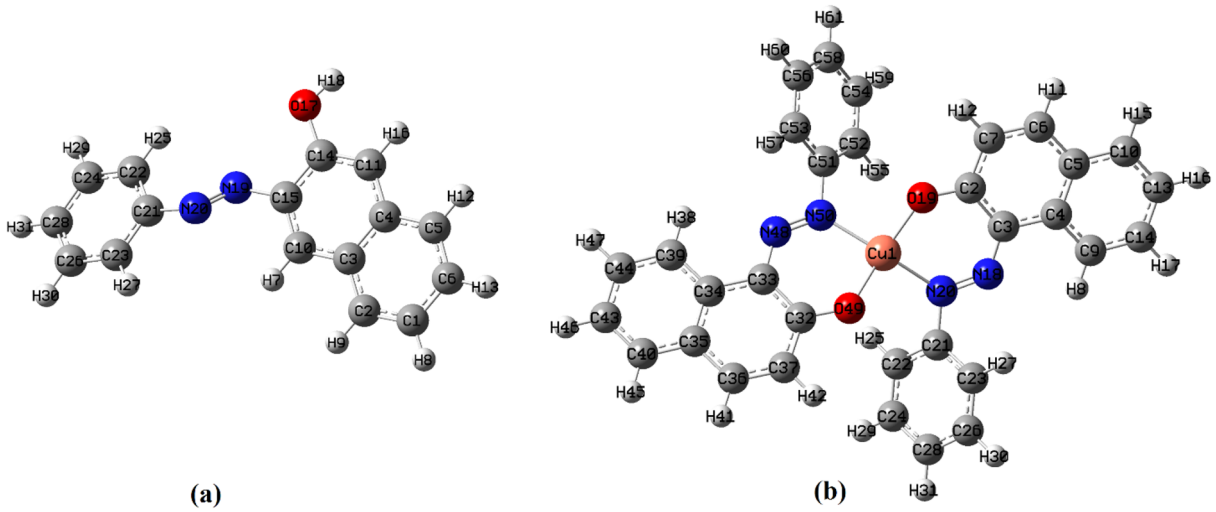

Fig. 9 Optimized structure of HL^1 and its Cu(II) complex, **a** HL^1 **b** $[Cu(L^1)_2].H_2O$ complex

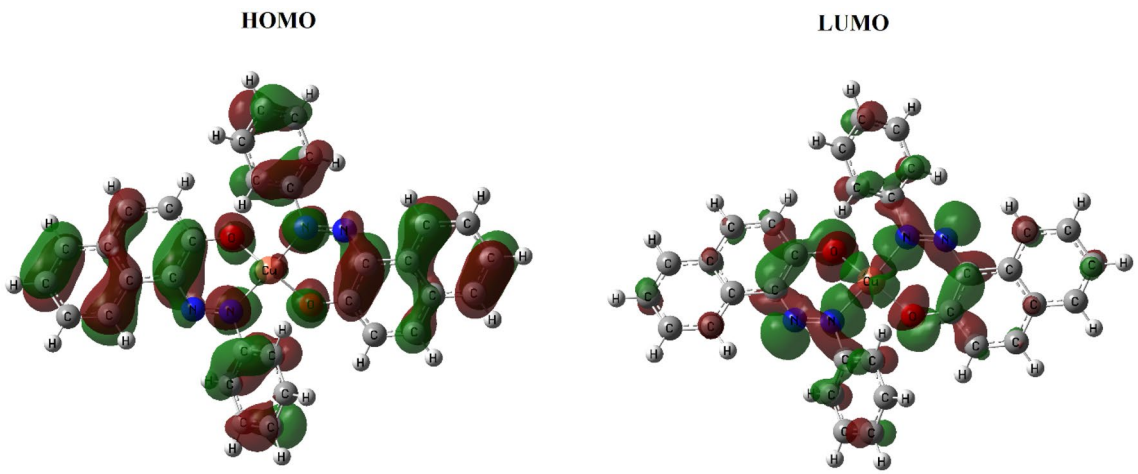

Fig. 10 The HOMO and LUMO of $[Cu(L^1)_2].H_2O$ complex

(μ), global hardness (η), softness (S) and electrophilicity index (ω) are shown in Table 3. Generally, the energy gap between HOMO and LUMO is an index for the reactivity of the compounds; such that, molecules with the least energy gap are soft and more reactive towards the metal ions and biological receptors compared to those having high values of energy gap [42]. According to the energy gap values of the studied ligands (Table 3), HL^2 is chemically more reactive than HL^1. Also, the other calculated molecular parameters; χ, μ, η, S and ω point to the same order of reactivity. Furthermore, the calculated energy gap for the $[Cu(L^1)_2].H_2O$ complex (Fig. 9) is quite small (1.594 eV) and hence, this complex is expected to possess some biological activity. Worth to mention that the low dipole moment of all complexes indicates their higher lipophilicity than the corresponding free ligand [43].

3.2.2 Molecular Electrostatic Potential (MEP)

The preferable sites for electrophilic and nucleophilic chemical interactions of a compound can be predicted by constructing the electrostatic potential map on its surface [44]. The color gradually alters from red which represents the regions with high electron density to blue which indicates the regions with electron deficiency. Figures 11 and S23 illustrate the molecular electrostatic potentials of HL^1, HL^2, and $[Cu(L^1)_2].H_2O$ complex. For instance, the most negative potential sites in HL^1 are N(19) and N(20) of the azo group, whereas, the positive potentials are on the hydrogen atoms of the rings with the most electrophilic site on H(18) (Fig. 11a). In the same manner, the active nucleophilic sites are located on the electronegative atoms O(25), O(28) and O(29) in HL^2 (Fig. 11c). Also, the low negative potential on the azo group of HL^2 ruled out its possibility of being a site of coordination with the metal ion which is in good harmony with the spectral data of the current research. Finally, constructing MEP for biologically active metal complexes is an important step in the drug designing procedure. Allocating the nucleophilic and electrophilic centers may shed light on their possible behavior with the cell membrane of microorganisms [44]. $[Cu(L^1)_2].H_2O$ complex showed a positive electrostatic potential on the metal core whereas the negative potentials are found in the outer region of the complex (Fig. S23).

3.2.3 Molecular Docking of Complexes

The activity of the synthesized metal complex as possible antipathogenic agents was estimated by molecular docking against three receptors: 1bqb, 3t88, and 4esw corresponding to *S. Aureus*, *E. Coli*, and *C. Albicans* proteins respectively [21–23]. The designated pathogenic micro-organisms are Gram-positive, Gram-negative bacteria and fungi that appear on the surfaces of various objects and cause superficial infections of human skin as well as mucous membranes infections. The docking results are displayed in Tables 4, S6 and Figs. 12 & S24–S28. The investigations revealed a strong inhibition effect of the Cu(II) complex against the targeted proteins. However, a less repressive behavior against the three selected proteins was noticed for the HL^1 ligand. Clearly, the presence of Cu metal enhances the interaction effect with the receptors through the short metallic bonds of lengths 2.33, 2.31, and 2.20 Å (Table 4). This close ligand-receptor interaction offered high-scoring energy (S) of values − 5.9267, − 6.8319, and − 7.3764 kcal/mol respectively. Nevertheless, the interaction with the receptor amino acids also includes ionic bond types involving N(20) and N(50) binding sites of the complex. The accountable binding receptors are Aspartate 216 in 1bqb, Glutamate 50 in 4esw, and Aspartate 197 in 3t88 protein. On the other hand, HL^1 showed side-chain donor activity toward acidic receptor (Glutamate 145) in 1bqb and side-chain acceptor activity toward basic receptor (Lysine 62) in 4esw (Fig. S24). Also, the best docking poses (Fig. 12b) revealed high ligand occlusion in the electronic cloud of the protein surface that points to high interaction efficiency and great inhibition activity toward the selected pathogens. The simulated antipathogenic activity of the Cu(II) complex is in agreement with similar reported Cu(II) complexes [45, 46] and hence was satisfactory to perform the *in vitro* biological activity which

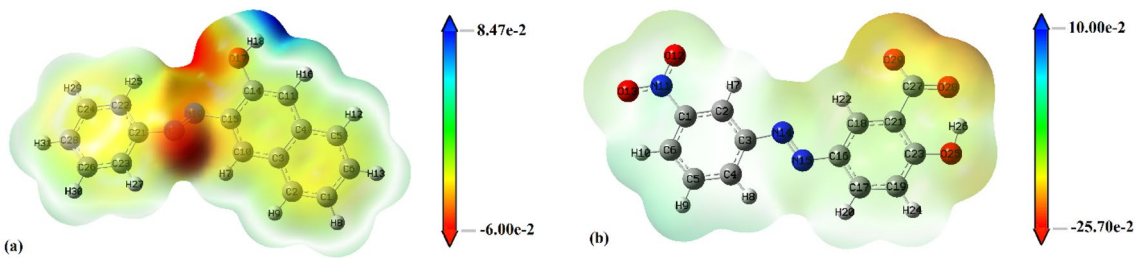

Fig. 11 Molecular electrostatic potential map of **a** HL^1 and **b** HL^2

Table 4 The docking parameters of HL^1 and its metal complexes, against 1bqb, 3t88 and 4esw proteins

Complex	Receptor	Ligand	Receptor	Interaction	Distance (Å)	E (kcal/mol)	S (kcal/mol)
HL^1	1bqb	O (17)	GLU 145	H-donor	3.30	− 1.1	− 5.1020
		C (23)	HIS 144	π-H	4.44	− 1.3	
	4esw	N(20)	LYS 62	H-acceptor	3.10	− 1.7	− 6.1341
	3t88	6-ring	MET 198	π-H	3.99	− 0.7	− 5.9277
$[Cu(L^1)_2]$	1bqb	Cu (1)	ASP 216	Metal	2.33	− 0.9	− 5.9267
		N (20)	ASP 216	Ionic	2.99	− 4.5	
		N (50)	ASP 216	Ionic	2.87	− 5.3	
	4esw	Cu (1)	GLU 50	Metal	2.31	− 1.2	
		N (20)	GLU 50	Ionic	2.67	− 7.1	− 6.8319
		N (50)	GLU 50	Ionic	3.05	− 4.2	
	3t88	Cu (1)	ASP 197	Metal	2.20	− 1.4	− 7.3764
		N (20)	ASP 197	Ionic	2.78	− 6.1	
		N (50)	ASP 197	Ionic	2.98	− 4.8	
$[Cu(L^1)_2].H_2O$	1bqb	C (5)	GLU 145	H-donor	3.55	− 0.7	− 5.8516
	4esw	N (19)	GLU 50	Ionic	3.22	− 3.1	− 6.6237
		N (49)	GLU 50	Ionic	2.96	− 4.7	
	3t88	6-ring	ILE 174	π-H	3.99	− 1.0	− 6.3274
		6-ring	LEU 236	π-H	3.80	− 0.6	
$[Ni(L^1)_2].H_2O$	1bqb	6-ring	ALA 115	π-H	4.13	− 0.8	− 6.0332
		6-ring	HIS 228	π-π	3.60	− 0.6	
	4esw	N (19)	GLU 50	Ionic	3.20	− 3.3	− 6.1777
		N (49)	GLU 50	Ionic	2.92	− 5.0	
	3t88	N (17)	ASN 202	H-acceptor	3.23	− 1.2	− 6.4804
		6-ring	LEU 236	π-H	3.69	− 0.8	

is displayed below. On the other hand, longer interaction distances with amino acids were observed for the complexes $[Co(L^1)_2].H_2O$ and $[Ni(L^1)_2].H_2O$ which results in less scoring energy compared to $[Cu(L^1)_2].H_2O$.

3.3 Antimicrobial Assay of the Synthesized Metal Complexes

The synthesized metal complexes were screened for their activity of inhibition against one Gram-positive (*S. Aureus*), one Gram-negative (*E. Coli*) and two fungi (*C. Albicans* and *A. Flavus*) utilizing the diffusion agar technique [11, 18]. The comparison between the inhibition zone diameter values of the synthesized complex with the standard drug values of Amphotericin B & Ampicillin (Table 5) suggests that HL^1 complexes possess moderate to significant antibacterial activity towards the tested organisms. The inhibition zone diameters exerted by this class of complexes were in the range 13.2–19.6, 16.6–20.3 and 15.1–18.8 mm/mg for the studied strains *C. Albicans*, *S. Aureus* and *E. Coli* respectively. Notably, Cu(II) complex showed more inhibitory effects than its free ligand HL^1. The superior biological activity of the complexes relative to their precursor ligands is very common and can be explained by Tweedy's chelation theory [47], where the chelation between the metal ion and the ligand causes a decrease in the polarity of the chelate by delocalization of the π electrons [48]. The allocation of electrons over the entire complex surface enhances its lipophilicity and hence its penetration capability through the phospholipid bilayer membrane of the biological cells [49]. Moreover, metal ions disturb the transfer of electrons in the electron transport chain by acting as terminal electron acceptors within the microbial cell [50, 51]. No activity was observed against *A. Flavus*. The yielded data of the isolated $[Cu(L^1)_2].H_2O$ complex proposed its antipathogenic potency against the tested strains. However, the less potency of HL^1 could be due to its higher polarity that was predicted theoretically which led to unsuccessful disperse through the bacterial cell wall or probably as a result of inactivation of HL^1 by certain bacterial enzymes [52]. Moreover, among HL^1 metal complexes, $Cu(L^1)$ exhibited the most potent inhibition activity. Clearly, Co(II) and Ni(II) complexes of the same geometries and stoichiometries as Cu(II) complexes showed less potency against the same species, implying the importance of the type of metal and its radius on the biological efficiencies of complexes. Additionally, metal complexes of HL^2 displayed less biological activity than the corresponding HL^1 complexes which could be attributed to the impact of geometrical and molecular size on the antimicrobial performance. Furthermore, Fe(III) complex was

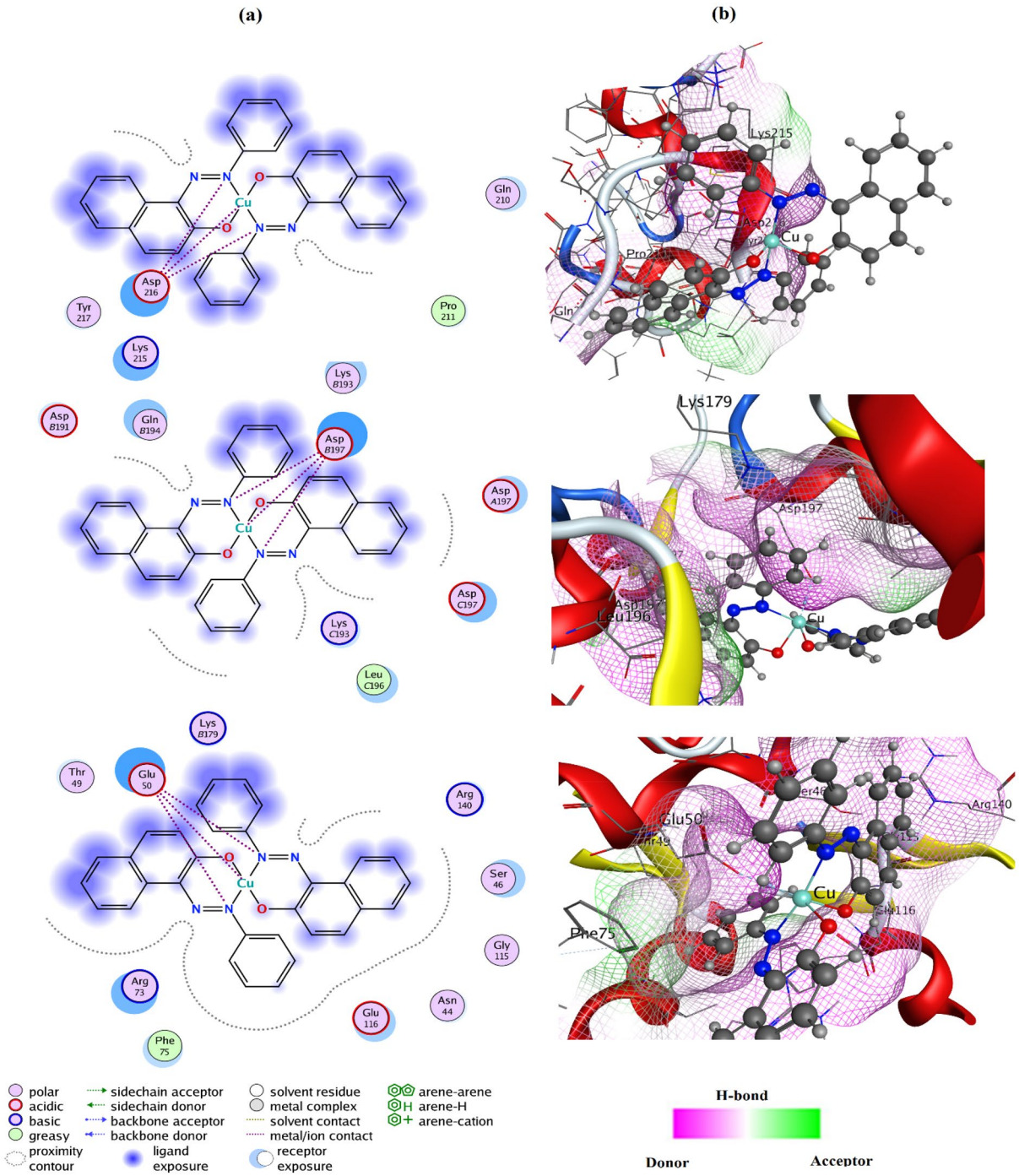

Fig. 12 The binding model **a** and the receptor surface map **b** of $[Cu(L^1)_2].H_2O$ complex against 1bqb, 3t88, and 4esw proteins

the only compound that exhibited inhibition activity against *A. Flavus* where the superior behavior could be provoked by the redox activity of Fe(III) complexes which facilitate oxidative cell damage.

4 Conclusion

Seven new azo -Fe(III), Co(II), Ni(II), and Cu(II) transition metal complexes were synthesized and characterized by different spectroscopic techniques (IR, UV-Vis., mass spectra, magnetism, and ESR) and thermal analysis (TGA, DTA, and DSC). A molar ratio of 1:2 (M:L)

Table 5 Antimicrobial activity of HL^1 and the synthesized complexes

Compounds	Inhibition zone diameter (mm / mg Sample)			
	C. Albicans	*A. Flavus*	*S. Aureus*	*E.Coli*
DMSO	–	–	–	–
HL^1	15.3 ± 0.2	–	16.9 ± 0.2	12.9 ± 0.4
$[Cu(L^1)_2].H_2O$	19.6 ± 0.3	–	20.3 ± 0.5	18.8 ± 0.7
$[Co(L^1)_2].H_2O$	12.0 ± 0.4	–	16.6 ± 0.8	15.1 ± 0.3
$[Ni(L^1)_2].H_2O$	13.2 ± 0.1	–	19.7 ± 0.8	17.9 ± 0.7
$[Fe(HL^2)_3].H_2O$	15.1 ± 0.4	7.3 ± 0.1	17.5 ± 0.5	16.2 ± 0.6
$[Co(HL^2)_2(H_2O)_2].H_2O$	11.8 ± 0.9	–	14.0 ± 0.2	15.4 ± 0.6
$[Ni(HL^2)_2(H_2O)_2].4H_2O$	15.7 ± 0.5	–	14.3 ± 0.5	15.9 ± 0.7
$[Cu(HL^2)_2].2H_2O$	13.8 ± 1.1	–	17.5 ± 0.7	18.6 ± 0.9
Ampicillin	–	–	21.4 ± 0.7	25.0 ± 1.0
Amphotericin B	25.4 ± 0.6	17.7 ± 1.2	–	–

was isolated for all complexes except the Fe (III) complex which exhibited a ratio of (1:3). Based on the data obtained from different measurements, square planar or octahedral geometries were the proposed structures for the studied complexes. ESR of Cu(II) complexes showed an anisotropic spectrum and pointed to the existence of exchange interaction between the Cu(II) centers. Additionally, all HL^1 metal complexes exhibited an extent of thermal stability up to ~ 300 ºC, implying their potential applications. DFT calculations of the bond angles confirmed a slight distortion of the square planar geometry of $[Cu(L^1)_2].H_2O$ that was proposed experimentally by ESR. Also, significant lipophilicity was predicted for all complexes compared to the free ligands. Molecular docking gave a good insight into the binding mode of the tested compounds with the adjacent amino acids inside the protein pocket. Among the metal complexes, Fe(III) complex showed the highest calculated scoring energy against the target proteins 1bqb, 3t88, and 4esw. The *in vitro* screening revealed moderate antimicrobial activity for some of the complexes, which assorted them as possible candidates for this purpose. In particular, $[Cu(L^1)_2].H_2O$ complex displayed appreciable activity against gram-positive *S. Aureus* and Fe(III) complex exhibited slight inhibition against *A. Flavus*.

Supplementary Information The online version contains supplementary material available at https://doi.org/10.1007/s10904-022-02483-x.

Acknowledgements The authors are grateful to Alexandria University, Egypt for supporting this investigation.

Funding Open access funding provided by The Science, Technology & Innovation Funding Authority (STDF) in cooperation with The Egyptian Knowledge Bank (EKB). The authors have not disclosed any funding.

Declarations

Conflict of interest The authors declare no competing financial interest.

References

1. H. Xu, X. Zeng, Synthesis of diaryl-azo derivatives as potential antifungal agents. Bioorg. Med. Chem. Lett. **20**, 4193–4195 (2010). https://doi.org/10.1016/j.bmcl.2010.05.048
2. A.Z. El-Sonbati, M.A. Diab, A.A. El-Bindary, A.F. Shoair, M.A. Hussein, R.A. El-Boz, Spectroscopic, thermal, catalytic and biological studies of Cu (II) azo dye complexes. J. Mol. Struct. **1141**, 186–203 (2017). https://doi.org/10.1016/j.molstruc.2017.03.082
3. A. Esme, S. Gunesdogdu Sagdinc, The vibrational studies and theoretical investigation of structure, electronic and non-linear optical properties of Sudan III [1-{[4-(phenylazo) phenyl]azo}-2-naphthalenol]. J. Mol. Struct. **1048**, 185–195 (2013). https://doi.org/10.1016/j.molstruc.2013.05.022
4. A. Airinei, M. Homocianu, D.O. Dorohoi, Changes induced by solvent polarity in electronic absorption spectra of some azo disperse dyes. J. Mol. Liq. **157**, 13–17 (2010). https://doi.org/10.1016/j.molliq.2010.07.011
5. S. Kamali, M. Orojloo, R. Arabahmadi, S. Amani, Design and synthesis of a novel azo-Schiff base ligand: its application as a colorimetric chemosensor for selective detection of Ni^{2+} and CN-in aqueous-organic media, computational studies, antimicrobial properties, and molecular logic circuits. J. Photochem. Photobiol. A: Chem. (2022). https://doi.org/10.1016/j.jphotochem.2022.114136
6. F.A. Saad, H.A. El-Ghamry, M.A. Kassem, A.M. Khedr, Nanosynthesis, Biological Efficiency and DNA binding affinity of new homo-binuclear metal complexes with sulfa azo dye based ligand for further pharmaceutical applications. J. Inorg. Organomet. Polym. Mater. **29**(4), 1337–1348 (2019). https://doi.org/10.1007/s10904-019-01098-z
7. N.V. Roik, L.A. Belyakova, M.O. Dziazko, Optically transparent silica film with pH-sensing properties: Influence of chemical immobilization and presence of β-cyclodextrin on protolytic properties of alizarin yellow. Sens. Actuators B: Chem. **273**, 1103–1112 (2018). https://doi.org/10.1016/j.snb.2018.07.033

8. M. Nehser, J. Dark, D. Schweitzer, M. Campbell, J. Zwicker, D.M. Hitt, H. Little, A. Diaz-Correa, D.C. Holley, S.A. Patel, C.M. Thompson, System X−c antiporter inhibitors: azo-linked amino-naphthyl-sulfonate analogues of sulfasalazine. Neurochem. Res. **45**, 1375–1386 (2020). https://doi.org/10.1007/s11064-019-02901-6
9. Y.Z. Zhang, J. Dai, X.P. Zhang, X. Yang, Y. Liu, Studies of the interaction between Sudan I and bovine serum albumin by spectroscopic methods. J. Mol. Struct. **888**, 152–159 (2008). https://doi.org/10.1016/j.molstruc.2007.11.043
10. M.S. Masoud, R.M.I. Elsamra, S.S. Hemdan, Solvent, substituents and pH effects towards the spectral shifts of some highly colored indicators. J. Serb. Chem. Soc. **82**, 851–864 (2017). https://doi.org/10.2298/JSC170204032M
11. M.S. Masoud, A.A. Soayed, S.A. Almesmari, R.M.I. Elsamra, New mixed-ligand complexes of cytosine and its silver nanoparticles: spectral, analytical, theoretical and biological activity studies. J. Inorg. Organomet. Polym. Mater. **31**, 2842–2858 (2021). https://doi.org/10.1007/s10904-021-01945
12. M.M. Khalil, A.H. El-Sayed, M.S. Masoud, E.M. Mahmoud, M.A. Hamad, Synthesis and optical properties of alizarin yellow GG-Cu(II)-PVA nanocomposite film as a selective filter for optical applications. J. Mater. Res. Technol. **11**, 33–39 (2021). https://doi.org/10.1016/j.jmrt.2020.12.105
13. A.M. Ramadan, R.M.I. Elsamra, S. Bondock, New pyrazole-4-carbothioamide-based metal complexes: synthesis, spectral characterization, computational, antimicrobial, and antitumor investigations. Appl. Organomet. Chem. **35**(2), e6102 (2021). https://doi.org/10.1002/aoc.6102
14. A.M. Ramadan, H.A. Bayoumi, R.M.I. Elsamra, Synthesis, characterization, biological evaluation, and molecular docking approach of nickel (II) complexes containing O, N-donor chelation pattern of sulfonamide-based Schiff bases. Appl. Organomet. Chem. **35**(12), e6412 (2021). https://doi.org/10.1002/aoc.6412
15. N. Venugopal, G. Krishnamurthy, H.S. Bhojya Naik, J.D. Manohara, DNA binding, molecular docking and antimicrobial evaluation of novel azo dye ligand and their metal complexes. J. Inorg. Organomet. Polym. Mater. **30**(7), 2608–2625 (2020). https://doi.org/10.1007/s10904-019-01394-8
16. A. Alharbi, A. Alsoliemy, S.O. Alzahrani, K. Alkhamis, S.J. Almehmadi, M.E. Khalifa, R. Zaky, N.M. El-Metwaly, Green synthesis approach for new Schiff's-base complexes; theoretical and spectral based characterization with in-vitro and in-silico Screening. J. Mol. Liq. **345**, 117803 (2022). https://doi.org/10.1016/j.molliq.2021.117803
17. C.J. O'Connor, in *Progress in Inorganic Chemistry*. ed. by S.J. Lippard (Wiley, Hoboken, 1982)
18. X. Sáez-Llorens, G.H. McCracken, in *Infectious diseases of the fetus and newborn infant*, Clinical Pharmacology of Antibacterial Agents (Elsevier Inc., 2006) pp. 1223–1267. https://doi.org/10.1016/B0-72-160537-0/50039-6
19. L. Borgese, A. Zacco, E. Bontempi, M. Pellegatta, L. Vigna, L. Patrini, L. Riboldi, F.M. Rubino, L.E. Depero, Use of total reflection X-ray fluorescence (TXRF) for the evaluation of heavy metal poisoning due to the improper use of a traditional ayurvedic drug. J. Pharm. Biomed. Anal. **52**, 787–790 (2010). https://doi.org/10.1016/j.jpba.2010.02.030
20. J.M. Ramos, O. Versiane, J. Felcman, C.A.S. Téllez, FT-IR vibrational spectrum and DFT:B3LYP/6–31G and B3LYP/6–311G structure and vibrational analysis of glycinate guanidoacetate nickel (II) complex: [Ni(Gly)(Gaa)]. Spectrochim. Acta A Mol. Biomol. Spectrosc. **72**, 182–189 (2009). https://doi.org/10.1016/j.saa.2008.09.026
21. A. Banbula, J. Potempa, J. Travis, C. Fernandez-Catalán, K. Mann, R. Huber, W. Bode, F.J. Medrano, Amino-acid sequence and three-dimensional structure of the *Staphylococcus aureus* metalloproteinase at 1.72 Å resolution. Structure **6**, 1185–1193 (1998). https://doi.org/10.1016/S0969-2126(98)00118-X
22. H.J. Li, X. Li, N. Liu, H. Zhang, J. Truglio, S. Mishra, C. Kisker, M. Garcia-Diaz, P. Tonge, Mechanism of the intramolecular claisen condensation reaction catalyzed by MenB, a crotonase superfamily member. Biochemistry **50**, 9532–9544 (2011). https://doi.org/10.1021/bi200877x
23. R.-Y. Lai, S. Huang, M.K. Fenwick, A. Hazra, Y. Zhang, K. Rajashankar, B. Philmus, C. Kinsland, J.M. Sanders, S.E. Ealick, T.P. Begley, Thiamin pyrimidine biosynthesis in Candida albicans: a remarkable reaction between histidine and pyridoxal phosphate. J. Am. Chem. Soc. **134**, 9157–9159 (2012). https://doi.org/10.1021/ja302474a
24. S. Suryana, M. Mutakin, Y. Rosandi, A.N. Hasanah, An update on molecularly imprinted polymer design through a computational approach to produce molecular recognition material with enhanced analytical performance. Molecules **26**, 1891 (2021). https://doi.org/10.3390/molecules26071891
25. P.Y. Bruice, *Organic chemistry*, 5th edn. (Pearson Education Inc, New Jersey, 2007)
26. N.M. Hosny, N.Y. Hassan, H.M. Mahmoud, M.H. Abdel-Rhman, Synthesis, characterization and cytotoxicity of new 2-isonicotinoyl-N-phenylhydrazine-1-carbothioamide and its metal complexes. Appl. Organomet. Chem. **33**, e4998 (2019). https://doi.org/10.1002/aoc.4998
27. A.M. Ramadan, A.A. Alshehri, S. Bondock, Synthesis, physicochemical studies and biological evaluation of new metal complexes with some pyrazolone derivatives. J. Saudi Chem. Soc. **23**, 1192–1205 (2019). https://doi.org/10.1016/j.jscs.2019.08.001
28. N.M. Hosny, M.A. Hussien, F.M. Radwan, N. Nawar, Synthesis, spectral characterization and DNA binding of Schiff-base metal complexes derived from 2-amino-3-hydroxyprobanoic acid and acetylacetone. Spectrochim. Acta A Mol. Biomol. Spectrosc. **132**, 121–129 (2014). https://doi.org/10.1016/j.saa.2014.04.165
29. Z. Warnke, C. Trojanowska, Copper(ii), Nickel(II) and Cobalt(II) Complexes of 2-Aminooxy acids and their esters. J. Coord. Chem. **21**, 1–11 (1990). https://doi.org/10.1080/00958979009408177
30. I.A. Mohammed, A. Mustapha, Synthesis of new azo compounds based on N- (4-Hydroxypheneyl) maleimide and N-(4-Methylpheneyl) maleimide. Molecules **15**, 7498–7508 (2010). https://doi.org/10.3390/molecules15107498
31. J.J. Max, C. Chapados, Infrared spectroscopy of aqueous carboxylic acids: comparison between different acids and their salts. J. Phys. Chem A. **108**, 3324–3337 (2004). https://doi.org/10.1021/jp036401t
32. M. Gaber, K.Y. El-Baradie, Y.S.Y. El-Sayed, Spectral and thermal studies of 4-(1H-pyrazolo 3,4-d pyrimidine-4-ylazo) benzene-1,3-diol complexes of cobalt(II), nickel(II) and copper(II). Spectrochim. Acta A Mol. Biomol. Spectrosc. **69**, 534–541 (2008). https://doi.org/10.1016/j.saa.2007.05.001
33. K.K. Narang, V.P. Singh, Synthesis and characterization of cobalt(II), nickel(II), copper(II) and zinc(II) complexes with acetylacetone bis-benzoylhydrazone and acetylacetone bis-isonicotinoyl hydrazone. Transition Met. Chem. **18**, 287–290 (1993). https://doi.org/10.1007/BF00207948
34. N. Novoa, F. Justaud, P. Hamon, T. Roisnel, O. Cador, B. Le Guennic, C. Manzur, D. Carrillo, J.-R. Hamon, Doubly phenoxide-bridged binuclear copper(II) complexes with ono tridentate schiff base ligand: synthesis, structural, magnetic and theoretical studies. Polyhedron **86**, 81–88 (2015). https://doi.org/10.1016/j.poly.2014.05.032
35. S. Chandra, L.K. Gupta, Electronic, EPR, magnetic and mass spectral studies of mono and homo-binuclear Co(II) and Cu(II) complexes with a novel macrocyclic ligand. Spectrochim Acta Part A Mol. Biomol. Spectrosc. **62**, 1102–1106 (2005). https://doi.org/10.1016/j.saa.2005.04.007

36. N.M. El Metwally, R. Arafa, U. El-Ayaan, Molecular modeling, spectral, and biological studies of 4-formylpyridine-4 N-(2-pyridyl) thiosemicarbazone (HFPTS) and its Mn(II), Fe(III), Co(II), Ni(II), Cu(II), Cd(II), Hg(II), and UO_2(II) complexes. J. Therm. Anal. Calorim. **115**, 2357–2367 (2014). https://doi.org/10.1007/s10973-013-3065-8
37. R. Prasad, A. Sulaxna, Kumar, Kinetics of thermal decomposition of iron(III) dicarboxylate complexes. J. Therm. Anal. Calorim. **81**, 441–450 (2005). https://doi.org/10.1007/s10973-005-0804-5
38. H.M. Abumelha, J.H. Al-Fahemi, I. Althagafi, A.A. Bayazeed, Z.A. Al-Ahmed, A.M. Khedr, N. El-Metwaly, Deliberate-characterization for Ni(II)-Schiff base complexes: promising in-vitro anticancer feature that matched MOE docking-approach. J. Inorg. Organomet. Polym. Mater. **30**, 3277–3293 (2020). https://doi.org/10.1007/s10904-020-01503-y
39. M.F. Coskun, K. Demirelli, D. Guzel, M. Coskun, Free-radical copolymerization of 3-phthalimido-2-hydroxypropyl methacrylate with styrene: the determination of monomer reactivity ratios and thermal analysis studies. J. Polym. Sci. Part A: Polym. Chem. **40**, 650–658 (2002). https://doi.org/10.1002/pola.10140
40. M.A. Khanfar, A.M. Jaber, M.A. Al-Damen, R.A. Al-Qawasmeh, Synthesis, characterization, crystal structure, and DFT study of a new square planar Cu(II) complex containing bulky adamantane ligand. Molecules **23**, 701 (2018). https://doi.org/10.3390/molecules23030701
41. T.A. Yousef, G.M.A. El-Reash, O.A. El-Gammal, S.F. Ahmed, Structural, DFT and biological studies on Cu(II) complexes of semi and thiosemicarbazide ligands derived from diketo hydrazide. Polyhedron **81**, 749–763 (2014). https://doi.org/10.1016/j.poly.2014.07.035
42. R. Srinivasaraghavan, S. Thamaraikannan, S. Seshadri, T. Gnanasambandan, Molecular conformational stability and spectroscopic analysis of Parared with experimental techniques and quantum chemical calculations. Spectrochim. Acta A Mol. Biomol. Spectrosc. **137**, 1194–1205 (2015). https://doi.org/10.1016/j.saa.2014.07.046
43. G.A.A. Al-Hazmi, K.S. Abou-Melha, N.M. El-Metwaly, I. Althagafi, F. Shaaban, R. Zaky, Green synthesis approach for Fe (III), Cu (II), Zn (II) and Ni (II)-Schiff base complexes, spectral, conformational, MOE-docking and biological studies. Appl. Organomet. Chem. **34**, e5403 (2020). https://doi.org/10.1002/aoc.5403
44. Y.M. Ahmed, W.H. Mahmoud, M.M. Omar, G.G. Mohamed, Synthesis, characterization and biological activity of transition metals schiff base complexes derived from 4,6-Diacetylresorcinol and 1,8-Naphthalenediamine. J. Inorg. Organomet. Polym. Mater. **31**, 2339–2359 (2021). https://doi.org/10.1007/s10904-020-01867-1
45. M. Habibi, S.A. Beyramabadi, S. Allameh, M. Khashi, A. Morsali, M. Pordel, M. Khorsandi-Chenarboo, Synthesis, experimental and theoretical characterizations of a new Schiff base derived from 2-pyridincarboxaldehyde and its Ni (II) complex. J. Mol. Struct. **1143**, 424–430 (2017). https://doi.org/10.1016/j.molstruc.2017.04.114
46. W.H. Mahmoud, M.M. Omar, Y.M. Ahmed, G.G. Mohamed, Transition metal complexes of Schiff base ligand based on 4,6-diacetyl resorcinol. Appl. Organometal. Chem. **34**, e5528 (2020). https://doi.org/10.1002/aoc.5528
47. T. Mosmann, Rapid colorimetric assay for cellular growth and survival: application to proliferation and cytotoxicity assays. J. Immunol. Methods **65**, 55–63 (1983). https://doi.org/10.1016/0022-1759(83)90303-4
48. N. Raman, R. Jeyamurugan, S. Sudharsan, K. Karuppasamy, L. Mitu, Metal based pharmacologically active agents: synthesis, structural elucidation, DNA interaction, *in vitro* antimicrobial and *in vitro* cytotoxic screening of copper(II) and zinc(II) complexes derived from amino acid based pyrazolone derivatives. Arab. J. Chem. **6**, 235–247 (2013). https://doi.org/10.1016/j.arabjc.2012.04.010
49. R. Neubert, Ion pair transport across membranes. Pharm. Res. **6**, 743–747 (1989). https://doi.org/10.1023/A:1015963128124
50. L. Gritsch, C. Lovell, W.H. Goldmann, A.R. Boccaccini, Fabrication and characterization of copper(II)-chitosan complexes as antibiotic-free antibacterial biomaterial. Carbohyd. Polym. **179**, 370–378 (2018). https://doi.org/10.1016/j.carbpol.2017.09.095
51. X. Ren, C. Yang, L. Zhang, S. Li, S. Shi, R. Wang, X. Zhang, T. Yue, J. Sun, J. Wang, Copper metal–organic frameworks loaded on chitosan film for the efficient inhibition of bacteria and local infection therapy. Nanoscale **11**, 11830–11838 (2019). https://doi.org/10.1039/C9NR03612A
52. G. Martinez de Tejada, S. Sánchez-Gómez, I. Rázquin-Olazaran, I. Kowalski, Y. Kaconis, L. Heinbockel, J. Andra, T. Schurholz, M. Hornef, A. Dupont, Bacterial cell wall compounds as promising targets of antimicrobial agents I. Antimicrobial peptides and lipopolyamines. Curr. Drug Targets **13**, 1121–1130 (2012). https://doi.org/10.2174/138945012802002410